

$L1_0$ FePd-Based Perpendicular Magnetic Tunnel Junctions with 65% Tunnel Magnetoresistance and Ultralow Switching Current Density

Deyuan Lyu^{1,*}, Jenae E. Shoup², Ali T. Habiboglu³, Qi Jia¹, Pravin Khanal³,
Brandon R. Zink¹, Yang Lv¹, Bowei Zhou³, Daniel B. Gopman², Weigang Wang³,
and Jian-Ping Wang¹

¹*Department of Electrical and Computer Engineering, University of Minnesota, Minneapolis, Minnesota 55455, USA*

²*Materials Science and Engineering Division, National Institute of Standards and Technology, Gaithersburg, Maryland 20899, USA*

³*Department of Physics, University of Arizona, Tucson, Arizona 85721, USA*

*Authors to whom correspondence should be addressed: lyu00039@umn.edu

$L1_0$ FePd is increasingly recognized as a potential candidate for magnetic tunnel junctions (MTJs), yet there remains room for enhancing device performance. In this work, we fabricated fully-integrated $L1_0$ FePd-based perpendicular MTJ devices and achieved a significant increase in tunnel magnetoresistance, reaching approximately 65%, compared to the previous record of 25%. Notably, we observed bi-directional switching with a low switching current density of about 1.4×10^5 A/cm², which outperforms the typical spin-transfer torque (STT) MTJ by about one order of magnitude. We propose two possible mechanisms to elucidate the switching process and associated device performance: 1) The voltage-controlled exchange coupling-driven switching of the bottom CoFeB layer; 2) The STT-driven switching of the exchange-coupled $L1_0$ FePd-CoFeB composite. While additional research is necessary, these findings may further advance the integration of $L1_0$ FePd into spintronic devices, potentially enabling low-energy memory and logic technologies.

The use of magnetic materials with perpendicular magnetic anisotropy (PMA) in magnetic tunnel junctions (MTJs) is pivotal for advancing spintronics-based memory and logic technologies.¹⁻⁷ As device sizes shrink to the single-digit nm scale,^{8,9} the traditional CoFeB material system, featured by its weak interfacial PMA ($K_{i,\text{CFB}} \sim 1.5$ mJ/m²), struggles to offer adequate thermal stability and non-volatility.^{10,11} Consequently, numerous other PMA materials—ranging from Co (or CoFe)-based multilayers¹²⁻¹⁵ and rare earth-transition metal compounds^{1,16,17} to $L1_0$ -phase alloys¹⁸⁻²⁰—have been explored for use as the free layer in MTJs. Among the various candidates, $L1_0$ FePd stands out due to its robust bulk PMA ($K_{b,\text{FePd}} \sim 1.7$ MJ/m³)^{21,22} and low Gilbert damping constant ($\alpha = 0.002-0.008$).²³⁻²⁶ More importantly, $L1_0$ FePd has been identified as a key material for voltage-controlled exchange coupling (VCEC) – an innovative MTJ switching mechanism that boasts reduced energy consumption.^{27,28} Moreover, the recently discovered interfacial PMA at the $L1_0$ FePd-Graphene interface underscores the potential synergies between $L1_0$ FePd and 2D material systems.²⁹ Furthermore, by using appropriate buffer and seed layers, high-quality $L1_0$ FePd thin films can be produced on industry-ready Si/SiO₂ wafers.³⁰ Despite the broad prospect of $L1_0$ FePd, integrating it into MTJ is non-trivial. For example, Pd atoms have a propensity to diffuse upon post-annealing, compromising

the tunnel magnetoresistance (TMR) ratio of the device.³¹ In a prior study, we achieved a TMR of ~25% using $L1_0$ FePd-based PMA-MTJs.³² Yet, significant enhancements are needed to further harness the potential of $L1_0$ FePd in spintronic applications.

In this study, we fabricated nano-sized $L1_0$ FePd PMA-MTJs and achieved a markedly improved TMR ratio of up to 65% at room temperature. To attain such a reasonably high TMR, we employed an ultrathin Ru/Mo bilayer spacer to suppress the diffusion of Pd. Additionally, we recorded an ultralow switching current density, J_{sw} , of approximately 1.4×10^5 A/cm². This value is roughly one order of magnitude lower than what is typically observed with spin-transfer torque (STT) MTJs. Given the stack structure and the observed switching behaviors, we suggest two plausible mechanisms to elucidate the device's switching process. The first hypothesis revolves around VCEC, while the second postulates the magnetic reversal of a composite free layer. Recognizing the importance of both mechanisms, our findings, although requiring further investigation, can be viewed as a significant milestone in the advancement of high-performance $L1_0$ FePd PMA-MTJ devices.

The $L1_0$ FePd PMA-MTJ thin films were prepared on MgO(001) substrates by direct current and radio frequency magnetron sputtering. The stack is MgO subs./Cr (7.5)/Pt (8)/ $L1_0$ FePd (5)/Ru (0.5)/Mo (0.5–0.9)/Co₂Fe₆B₂ (1)/MgO (1.2)/Co₂Fe₆B₂ (1.5)/Ta (3)/Ru (8), in which the number in parentheses are the layer thickness in nm. In prior to the deposition, we annealed the substrate at 600°C for 60 min in vacuum and then 30 min in 0.8 mTorr of N₂. The sample was then cooled down to 350°C in the N₂ environment. The N₂ treatment is performed to heal the Oxygen vacancies generated on MgO surface during vacuum annealing.³³ Then, the Cr, Pt, and FePd layers were all grown at 350°C. After cooling the sample down to room temperature, we deposited a Ru (0.5) cap on top of the FePd layer. Given the constraints of our equipment with limited cathode sites, the vacuum was interrupted after depositing Ru (0.5) to transition the sample between sputtering systems.

Before loading the Ru (0.5)-capped thin films into the second sputter for the following deposition, a small piece of the sample was taken for X-ray diffraction (XRD) and ferromagnetic resonance (FMR) measurements to confirm the microstructure and magnetic properties of the FePd layer. The XRD θ - 2θ results were collected using a Rigaku SmartLab (Rigaku Corporation, Japan)³⁴ and plotted in Fig. 1(a). The (002) peaks from the Cr, Pt, and FePd layers as well as the (001) superlattice peak from FePd were observed on this sample. The full-width-at-half maximum was used as an estimate for the structural coherence length of each layer and the integral intensities of the FePd (002) and (001) peaks were used to estimate the degree of $L1_0$ order. The estimated structural coherence lengths for the (001) FePd peak and the (002) FePd, Pt, and Cr peaks were (in Å) 44.5(4), 44.3(12), 73.8(11), and 61.2(9), respectively. Numbers in parentheses reflect the one-sigma fitting error for the assembly of symmetric pseudo-Voigt fitting functions used to estimate the full-width-at-half maximum for each peak. The coherence length for the (001) and (002) FePd peaks were nearly identical, and more generally our estimate for the

coherence length of each layer came to within 10% of the nominal thickness value, for which the systematically lower values may be related to interfacial roughness. The $L1_0$ order parameter for FePd was estimated to be 0.677(22) based on the integrated intensities for the FePd (001) and FePd (002) peaks, revealing a moderate-high degree of superlattice ordering.

Broadband FMR spectra, as shown in Fig. 1(b), were recorded using a custom microwave stripline, a broadband generator and a diode detector, using a swept direct current magnetic field out-of-plane and a set of low-frequency (377 Hz) Helmholtz coils for lock-in detection of changes in the microwave absorption on resonance. Based on the frequency-resonance field (f - $\mu_0 H_{\text{res}}$) spectra shown in Fig. 1(c), the $L1_0$ FePd sample showed an effective perpendicular anisotropy field of 0.557(1) T. Measurements of the linewidth (ΔH)- f indicate an α of 0.0151(8), larger than the typical literature values,^{23,24} which can be understood from the significant spin pumping effect between the underlying Pt layer and the 5 nm thick FePd film. An inhomogeneous linewidth broadening of 0.0361(14) T was estimated as well, consistent with the large PMA and relatively broad mosaic spread of 2.87(12) degrees for the FePd(001) crystallites estimated from the XRD rocking curve (not shown). Mitigating the spin pumping with an insertion layer and/or reducing the FePd(001) mosaic spread are both clear opportunities to explore further materials optimization of the film stacking structure and processing conditions.

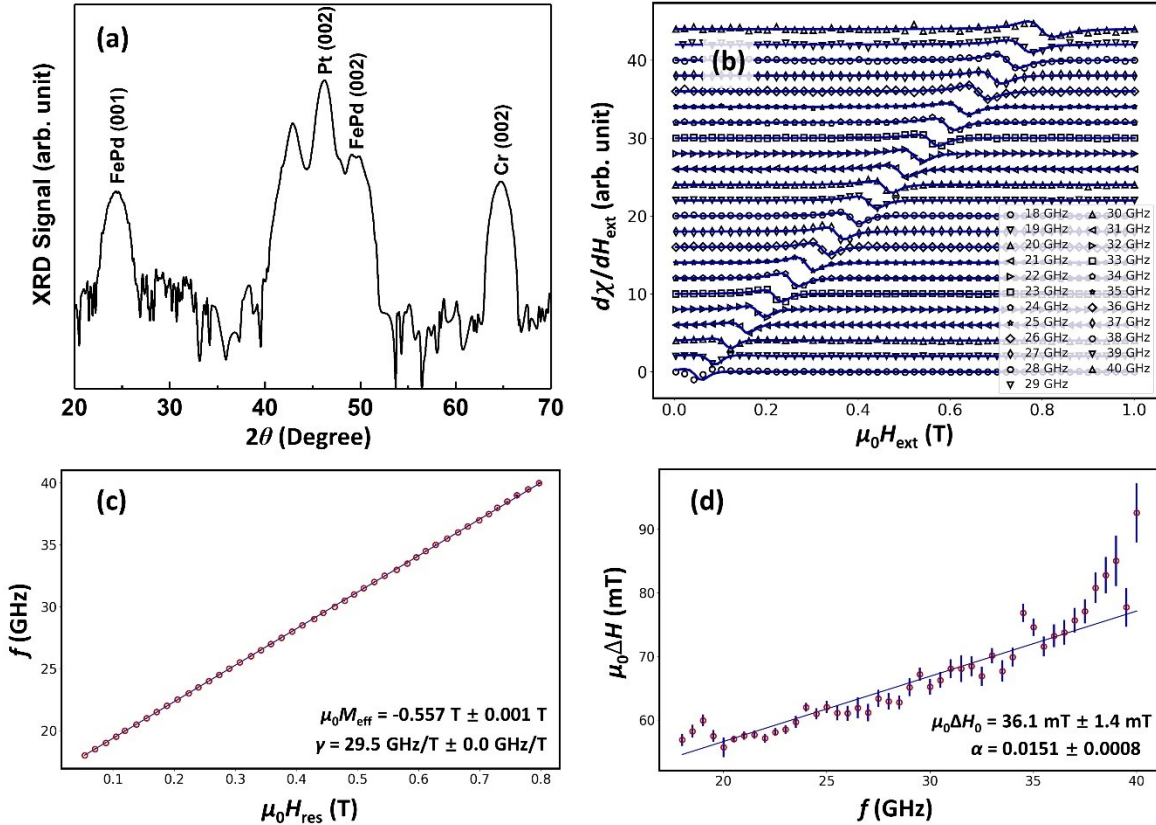


FIG. 1. (a) XRD θ - 2θ spectrum of the $L1_0$ FePd sample. (b) FMR spectra with f ranging from 18 GHz to 40 GHz. (c) and (d) Curve-fitting results of f vs. H_{res} and ΔH vs. f .

All the following layers, starting from Mo (0.5–0.9), were deposited at room temperature in the second sputter. The full stack structure is depicted in Fig. 2(a) and the arrow highlights the ultrathin Ru (0.5)/Mo (0.5–0.9) bilayer. We will further discuss its key role in influencing the device performance and functionality. After the completion of the layer deposition, the sample underwent post-annealing at 300°C for 10 min to induce the PMA of the CoFeB layers. The magnetization-external magnetic field (M - $\mu_0 H_{\text{ext}}$) loop, taken from a specimen cut from the sample's central region (with a Mo thickness of ~ 0.7 nm), was assessed under perpendicular fields using vibrating-sample magnetometry (VSM) and is presented in Fig. 2(b). The stack's PMA is evident, with a distinct two-step magnetization switching pattern emerging. Evaluating the magnetization and switching field for both events, it is plausible to infer that the low field switching (occurring around $\mu_0 H_{\text{SW}} \sim 5$ mT) is attributed to the magnetization reversal of the top CoFeB layer. Conversely, the high field switching (initiating at approximately 20 mT) signifies a synchronous reversal of both the bottom CoFeB and the FePd layers.

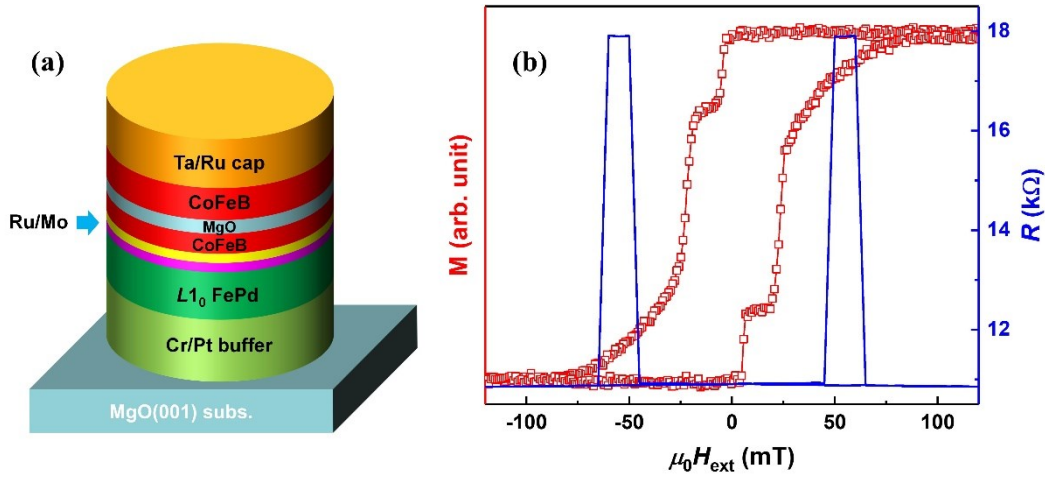


FIG. 2. (a) Schematic illustration of the stack structure of the L_{10} FePd PMA-MTJ sample. (b) M - H_{ext} loop of the unpatterned thin films (red line and squares) and major R - H_{ext} loop of a patterned device (blue line).

To study the magneto-transport properties of L_{10} FePd PMA-MTJs, we patterned the sample thin films into nanopillar devices by utilizing the combination of optical and e-beam lithography techniques and Ar^+ ion milling. These devices have a pillar diameter of 300 nm. Subsequent contact pads were fashioned through a liftoff process. As illustrated in Fig. 2(b), the resistance (R)- $\mu_0 H_{\text{ext}}$ loop reveals a TMR ratio of approximately 65%, marking a notable enhancement compared to previous results.³² In this context, the ultrathin Ru/Mo bilayer is leveraged as a diffusion barrier for Pd atoms, contributing to the enhanced TMR. It is worth noting that the switching fields evident in the R - $\mu_0 H_{\text{ext}}$ loop are considerably greater than those in the M - $\mu_0 H_{\text{ext}}$ loop. This discrepancy can be attributed to alterations in dipolar interaction and shape anisotropy.

To delve deeper into the electrical characteristics of L_{10} FePd PMA-MTJ devices, we recorded resistance (R) as a function of current (I) under varying offset fields. As depicted by the red line in Fig. 3, pronounced bi-directional switching events

emerge when $\mu_0 H_{\text{ext}}$ is set to -26.5 mT. Remarkably, we observed a switching current of approximately 100 μA , yielding an ultralow switching current density (J_{SW}) of around $1.4 \times 10^5 \text{ A/cm}^2$. Such a small J_{SW} is approximately one order of magnitude lower compared with that of typical STT MTJs³⁵ and highly advantageous for the widespread application of spintronic devices. It is worth pointing out that the resistance-area (RA) product of our $L1_0$ FePd PMA-MTJ devices exceeds $600 \Omega \cdot \mu\text{m}^2$. This is considerably larger than typical STT MTJs whose RA product is in the range of $10 \Omega \cdot \mu\text{m}^2$ or so with the MgO barrier of about 1 nm or even thinner. Given this context, it seems improbable that the observed switching is driven purely by STT with such a small J_{SW} .

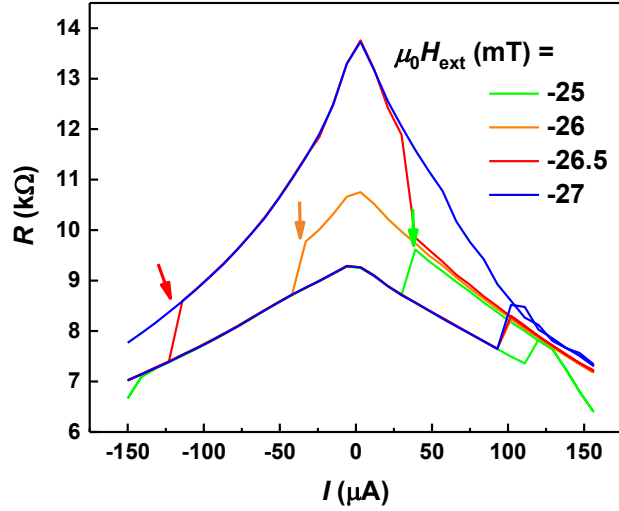


FIG. 3. R - I loops of a $L1_0$ FePd PMA-MTJ device under different H_{ext} . The AP-to-P J_{SW} values are marked by arrows.

It is worth mentioning the resistive switching mechanism, for which the change in device resistance usually stem from the formation and rupture of conducting filaments,^{36,37} is also reported with MgO as the functional layer.³⁸⁻⁴⁰ To further investigate the switching mechanism of the $L1_0$ FePd PMA-MTJ devices, we made minor adjustments to the offset field and plotted the resultant resistance-current (R - I) loops in Fig. 3 for comparative analysis. As denoted respectively by the green and orange lines, with a lower offset field of -25 mT and -26 mT, the antiparallel (AP)-to-parallel (P) J_{SW} is significantly reduced. These J_{SW} values are marked by arrows. In contrast, as showcased by the blue line, with a larger offset field of -27 mT, the AP-to-P switching becomes absent. The P-to-AP J_{SW} , however, exhibits a lesser dependency on H_{ext} . In addition, the full AP state is not realized with lower offset fields, which is probably caused by domain wall pinning. Clearly, the switching behavior is highly sensitive to H_{ext} . As a result, the resistive switching mechanism can be ruled out. In other words, the detected R change is attributed to the TMR of the MTJ nanopillar.

Based on the stack structure, device performance, and switching characteristics, we believe the bi-directional ultralow- J_{SW} switching can be explained by the driven of VCEC, as illustrated in Fig. 4(a). Specifically, the voltage applied instigates an

electric field (E-field) capable of modulating the interlayer exchange coupling (IEC) between the $L1_0$ FePd layer and the bottom CoFeB layer. Unlike the traditional voltage-controlled magnetic anisotropy effect,^{41,42} which has been extensively investigated and where the E-field impacts only the local electronic structure within a few atomic layers,⁴³ the VCEC effect manifests a longer range. This is because the Ruderman–Kittel–Kasuya–Yosida (RKKY) interaction is dependent on the electron wave functions in the ferromagnets. Though the E-field is confined to the bottom CoFeB-MgO interface due to Debye screening, it can still modulate the phases of up and down spins across the entire CoFeB layer. This modulation affects the RKKY IEC with the $L1_0$ FePd layer.²⁷ With a sufficiently strong VCEC effect, the IEC could even be changed from ferromagnetic to anti-ferromagnetic or vice versa. When the reversed IEC achieves a certain magnitude, the magnetization of the bottom CoFeB can be switched. Previously, the VCEC-driven switching has been reported in the $L1_0$ FePd-CoFeB system, showcasing a similarly low J_{SW} of $\sim 1.1 \times 10^5$ A/cm².²⁵ Considering that the ultrathin Ru layer may mediate a strong anti-ferromagnetic IEC and the insertion of an extra ultrathin spacer can substantially weaken the coupling strength,^{44,45} the Ru/Mo bilayer spacer in the present study should mediate a relatively weaker IEC, which can have its polarity altered through VCEC.

Given the large RA product and ultralow J_{SW} , we speculate that STT is insufficient to drive the switching process. In the VCEC switching discussed above, the free layer is the bottom CoFeB layer, and the $L1_0$ FePd layer plays a role primarily through its interaction with the CoFeB layer via the ultrathin Ru/Mo bilayer spacer. Nonetheless, quantitative evidence is still needed to support this assumption. By assuming STT as the dominating driven force, the switching process can be understood through the formation of a composite free layer, as shown in Fig. 4(b). When measuring R - I loops, the electrons flow from the top contact to the bottom suggests AP-to-P switching, indicating that the free layer is beneath the MgO tunnel barrier. As the bottom CoFeB layer and the FePd layer switch synchronously in the M - H_{ext} loop, it is reasonable to believe that the two layers are tightly coupled through the ultrathin Ru/Mo bilayer spacer and can effectively act as a composite free layer. Compared with the VCEC switching of the CoFeB, the STT switching of the $L1_0$ FePd-CoFeB composite requires not merely a large STT at

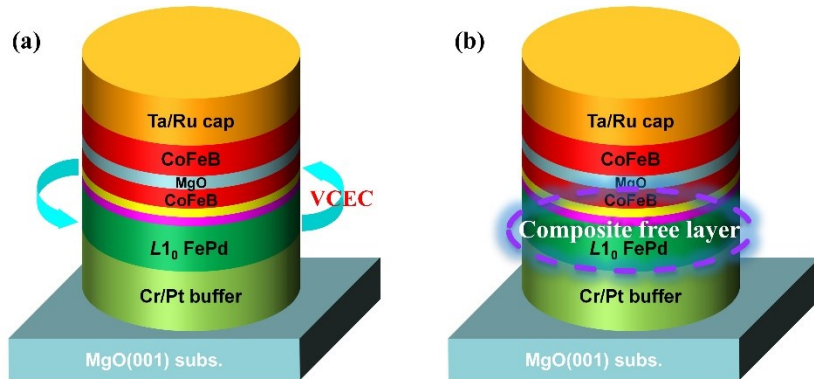


FIG. 4. Two possible switching mechanisms of our $L1_0$ FePd PMA-MTJ devices. (a) VCEC-driven switching of the bottom CoFeB layer. (b) STT-driven switching of the $L1_0$ FePd-CoFeB composite.

ultralow J_{SW} , but also a strong IEC within the free layer composite. In future studies, comprehensive research will be essential to conclusively determine the switching mechanism in our $L1_0$ FePd PMA-MTJ devices.

It is worth mentioning that besides the two switching mechanisms discussed above, the STT switching of the bottom CoFeB layer may also be dominating. It is often reported that two layers coupled in the unpatterned sample could decouple from each other after being patterned into nanoscale devices.³⁵ Thus, the bottom CoFeB layer may decouple from the $L1_0$ FePd layer after device patterning and undergo STT switching independently. Nonetheless, in this switching process, the magnetization of the FePd layer is expected to impact the switching characteristics, at least in the form of the stray field. As we did not observe any dependence of the offset field on the field-sweeping history, this trivial switching process is less possible.

In conclusion, we have successfully fabricated nano-sized $L1_0$ FePd PMA-MTJ devices, achieving an enhanced TMR of up to 65%—a considerable leap from the prior record of 25%. VSM results confirmed the PMA of the stack and showed two switching steps, which respectively correspond to the top CoFeB layer and the composite of the bottom CoFeB layer and the $L1_0$ FePd layer. Surprisingly, electrical-driven bi-directional switching was observed with an ultralow J_{SW} of $\sim 1.4 \times 10^5$ A/cm², which is about one order of magnitude lower than that of typical STT-MTJs. To ensure that the switching is associated with magnetization reversal, we verified the H_{ext} -sensitivity of the switching characteristics and thus possibility of resistive switching should be excluded. Based on the sample stack structure and device performance, two possible switching mechanisms were proposed. One is the VCEC-driven switching of the bottom CoFeB layer, in which its IEC with the $L1_0$ FePd layer can be modified via voltage. The other is the STT-driven switching of the $L1_0$ FePd-CoFeB composite, in which the two layers switch together and serve as the free layer. These results shed light on the application of $L1_0$ FePd as an important material choice in PMA MTJs and offer promising directions for the development of spintronics-based memory and logic devices with ultralow energy consumption.

This work was supported in part by the Defense Advanced Research Projects Agency (DARPA) (Advanced MTJs for computation in and near random access memory) under Grant HR001117S0056-FP-042, in part by the National Institute of Standards and Technology (NIST), in part by the National Science Foundation (NSF) GOALI: Advancement of Heat-Assisted Magnetic Recording Enabled by Time-Resolved Magneto-Optical Kerr Effect Metrology under Grant 2226579, and in part by the Minnesota Nano Center by the NSF through the National Nanotechnology Coordinated Infrastructure (NNCI) under Award ECCS-202512.

The authors have no conflicts to disclose.

The data that support the findings of this study are available from the corresponding author upon reasonable request.

REFERENCES

- ¹N. Nishimura, T. Hirai, A. Koganei, T. Ikeda, K. Okano, Y. Sekiguchi, and Y. Osada, *J. Appl. Phys.* **91**, 5246 (2002).
- ²A. D. Kent, B. Özyilmaz, and E. del Barco, *Appl. Phys. Lett.* **84**, 3897 (2004).
- ³K. J. Lee, O. Redon, and B. Dieny, *Appl. Phys. Lett.* **86**, 022505 (2005).
- ⁴H. Meng and J.-P. Wang, *Appl. Phys. Lett.* **88**, 172506 (2006).
- ⁵S. Mangin, D. Ravelosona, J. A. Katine, M. J. Carey, B. D. Terris, and E. E. Fullerton, *Nat. Mater.* **5**, 210 (2006).
- ⁶J.-P. Wang, S. S. Sapatnekar, C. H. Kim, P. Crowell, S. Koester, S. Datta, K. Roy, A. Raghunathan, X. S. Hu, M. Niemier, A. Naeemi, C.-L. Chien, C. Ross, and R. Kawakami, in *Proc. 54th Annual Design Automation Conf. (DAC '17)*, Art. no. 16, Austin, TX, USA, June 2017.
- ⁷K. C. Chun, H. Zhao, J. D. Harms, T.-H. Kim, J.-P. Wang, and C. H. Kim, *IEEE J. Solid-State Circuits* **48**, 598 (2013).
- ⁸K. Watanabe, B. Jinnai, S. Fukami, H. Sato, and H. Ohno, *Nat. Commun.* **9**, 663 (2018).
- ⁹B. Jinnai, J. Igarashi, K. Watanabe, T. Funatsu, H. Sato, S. Fukami, and H. Ohno, in *Proc. IEEE Int. Electron. Devices Meeting (IEDM)*, San Francisco, CA, USA, December 2020.
- ¹⁰S. Ikeda, K. Miura, H. Yamamoto, K. Mizunuma, H. D. Gan, M. Endo, S. Kanai, J. Hayakawa, F. Matsukura, and H. Ohno, *Nat. Mater.* **9**, 721 (2010).
- ¹¹S. Peng, W. Kang, M. Wang, K. Cao, X. Zhao, L. Wang, Y. Zhang, Y. Zhang, Y. Zhou, K. L. Wang, and W. Zhao, *IEEE Magn. Lett.* **8**, 3105805 (2017).
- ¹²L. E. Nistor, B. Rodmacq, S. Auffret, and B. Dieny, *Appl. Phys. Lett.* **94**, 012512 (2009).
- ¹³K. Yakushiji, T. Saruya, H. Kubota, A. Fukushima, T. Nagahama, S. Yuasa, and K. Ando, *Appl. Phys. Lett.* **97**, 232508 (2010).
- ¹⁴B. Carvello, C. Ducruet, B. Rodmacq, S. Auffret, E. Gautier, G. Gaudin, and B. Dieny, *Appl. Phys. Lett.* **92**, 102508 (2008).
- ¹⁵Z. R. Tadisina, A. Natarajarathinam, and S. Gupta, *J. Vac. Sci. Technol. A* **28**, 973 (2010).
- ¹⁶M. Nakayama, T. Kai, N. Shimomura, M. Amano, E. Kitagawa, T. Nagase, M. Yoshikawa, T. Kishi, S. Ikegawa, and H. Yoda, *J. Appl. Phys.* **103**, 07A710 (2008).
- ¹⁷L.-X. Ye, C.-M. Lee, J.-H. Lai, A. Canizo-Cabrera, W.-J. Chen, and T.-h. Wu, *J. Magn. Magn. Mater.* **322**, L9 (2010).
- ¹⁸P. de Person, P. Warin, M. Jamet, C. Beigne, and Y. Samson, *Phys. Rev. B* **76**, 184402 (2007).
- ¹⁹G. Kim, Y. Sakuraba, M. Oogane, Y. Ando, and T. Miyazaki, *Appl. Phys. Lett.* **92**, 172502 (2008).
- ²⁰T. Kishi, H. Yoda, T. Kai, T. Nagase, E. Kitagawa, M. Yoshikawa, K. Nishiyama, T. Daibou, M. Nagamine, M. Amano, S. Takahashi, M. Nakayama, N. Shimomura, H. Aikawa, S. Ikegawa, S. Yuasa, K. Yakushiji, H. Kubota, A. Fukushima, M. Oogane, T. Miyazaki, and K. Ando, in *Proc. IEEE Int. Electron. Devices Meeting (IEDM)*, San Francisco, CA, USA, December 2008.
- ²¹T. Klemmer, D. Hoydick, H. Okumura, B. Zhang, and W. A. Soffa, *Scr. Metall. Mater.* **33**, 1793 (1995).
- ²²H. Zhao, (2013), Spin Transfer Torque Induced Switching In Magnetic Tunnel Junction For STT-RAM Application, Retrieved from the University of Minnesota Digital Conservancy, <https://hdl.handle.net/11299/177055>.
- ²³S. Iihama, A. Sakuma, H. Naganuma, M. Oogane, S. Mizukami, and Y. Ando, *Phys. Rev. B* **94**, 174425 (2016).
- ²⁴X. Wang, S. Krylyuk, D. Josell, D. Zhang, D. Lyu, J.-P. Wang, and D. B. Gopman, *AIP Adv.* **11**, 025106 (2021).
- ²⁵P. He, X. Ma, J. W. Zhang, H. B. Zhao, G. Lüpke, Z. Shi, and S. M. Zhou, *Phys. Rev. Lett.* **110**, 077203 (2013).
- ²⁶D. Huang, D. Lyu, X. Wang, M. B. Katz, D. Zhang, J.-P. Wang, D. B. Gopman, and X. Wang, *Phys. Rev. Mater.* **6**, 113402 (2022).
- ²⁷D. Zhang, M. Bapna, W. Jiang, D. Sousa, Y.-C. Liao, Z. Zhao, Y. Lv, P. Sahu, D. Lyu, A. Naeemi, T. Low, S. A. Majetich, and J.-P. Wang, *Nano Lett.* **22**, 622 (2022).
- ²⁸B. R. Zink, D. Zhang, H. Li, O. J. Benally, Y. Lv, D. Lyu, and J.-P. Wang, *Adv. Electron. Mater.* **8**, 2200382 (2022).
- ²⁹H. Naganuma, M. Nishijima, H. Adachi, M. Uemoto, H. Shinya, S. Yasui, H. Morioka, A. Hirata, F. Godel, M.-B. Martin, B. Dlubak, P. Seneor, and K. Amemiya, *ACS Nano* **16**, 4139 (2022).
- ³⁰D. Lyu, J. E. Shoup, D. Huang, J. García-Barriocanal, Q. Jia, W. Echtenkamp, G. A. Rojas, G. Yu, B. R. Zink, X. Wang, D. B. Gopman, and J.-P. Wang, *Adv. Funct. Mater.* **33**, 2214201 (2023).
- ³¹D.-L. Zhang, K. B. Schliep, R. J. Wu, P. Quarterman, D. Reifsnyder Hickey, Y. Lv, X. Chao, H. Li, J.-Y. Chen, Z. Zhao, M. Jamali, K. A. Mkhoyan, and J.-P. Wang, *Appl. Phys. Lett.* **112**, 152401 (2018).
- ³²D.-L. Zhang, C. Sun, Y. Lv, K. B. Schliep, Z. Zhao, J.-Y. Chen, P. M. Voyles, and J.-P. Wang, *Phys. Rev. Appl.* **9**, 044028 (2018).
- ³³I. Suzuki, S. Kubo, H. Sepehri-Amin, and Y. K. Takahashi, *ACS Appl. Mater. Interfaces* **13**, 16620 (2021).
- ³⁴Certain commercial equipment, instruments, or materials are identified in this paper in order to specify the experimental procedure adequately. Such identification is not intended to imply recommendation or endorsement by

NIST, nor is it intended to imply that the materials or equipment identified are necessarily the best available for the purpose.

³⁵D. Lyu, P. Khanal, Y. Lv, B. Zhou, H. Yun, Q. Jia, B. R. Zink, Y. Fan, K. A. Mkhoyan, W. Wang, and J.-P. Wang, *IEEE Electron Device Lett.* **43**, 1215 (2022).

³⁶C. Hu, Q. Wang, S. Bai, M. Xu, D. He, D. Lyu, and J. Qi, *Appl. Phys. Lett.* **110**, 073501 (2017).

³⁷Y. Yang, P. Gao, S. Gaba, T. Chang, X. Pan, and W. Lu, *Nat. Commun.* **3**, 732 (2012).

³⁸F.-C. Chiu, W.-C. Shih, and J.-J. Feng, *J. Appl. Phys.* **111**, 094104 (2012).

³⁹J. M. Teixeira, J. Ventura, R. Fermento, J. P. Araujo, J. B. Sousa, P. Wisniowski, and P. P. Freitas, *J. Phys. D: Appl. Phys.* **42**, 105407 (2009).

⁴⁰A. Schulman, E. Paz, T. Böhnert, A. S. Jenkins, and R. Ferreira, *Adv. Funct. Mater.* **33**, 2305238 (2023).

⁴¹W.-G. Wang, M. Li, S. Hageman, and C. L. Chien, *Nat. Mater.* **11**, 64 (2011).

⁴²Y. Shiota, T. Nozaki, F. Bonell, S. Murakami, T. Shinjo, and Y. Suzuki, *Nat. Mater.* **11**, 39 (2012).

⁴³J. Zhang, P. V. Lukashev, S. S. Jaswal, and E. Y. Tsybal, *Phys. Rev. B* **96**, 014435 (2017).

⁴⁴C. Yoshida, T. Takenaga, Y. Iba, Y. Yamazaki, H. Noshiro, K. Tsunoda, A. Hatada, M. Nakabayashi, A. Takahashi, M. Aoki, and T. Sugii, *IEEE Trans. Magn.* **49**, 4363 (2013).

⁴⁵D. Lyu, D. Zhang, D. B. Gopman, Y. Lv, O. J. Benally, and J.-P. Wang, *Appl. Phys. Lett.* **120**, 012404 (2022).